AIAA JOURNAL
Vol. 34, No. 12, December 1996

Tunnel-Induced Gradients and Their Effect on Drag

J. E. Hackett*
Lockheed Martin Aeronautical Systems Company, Marietta, Georgia 30060

A wake-induced drag increment is discussed that is independent of the horizontal buoyancy, gradient times volume, form usually used to correct wind-tunnel data. It is shown that the latter form should be used only in connection with externally imposed gradients. An analysis is provided that shows how, contrary to traditional thinking, products of image-induced gradients with volume-related quantities sum to zero. It is demonstrated experimentally that the size of a separation bubble can be reduced significantly by tunnel effects. The wake-induced drag increment corrects for this. Using experimental data, wake-induced drag increments are compared to, and found to agree well with, increments obtained using a modified version of Maskell's method. If derived using wall pressure methods, the wake-induced drag increment includes the changes in tunnel boundary-layer drag. A formulation is provided, using model viscous drag, that avoids this.

Nomenclature

B = tunnel width
C = tunnel cross-sectional area
C_{DcMW} = fully corrected drag coefficient using wall pressures and ΔC_{DMW} (Fig. 7)
C_{DcM1} = drag coefficient corrected using the standard Maskell method [Eq. (15) and Fig. 7]
C_{DcM2} = drag coefficient corrected using the two-stage Maskell method [Eq. (13) and Fig. 7]
$C_{DM\,vis}$ = measured or estimated viscous drag coefficient of model [Eq. (11)]
C_{Du} = uncorrected drag coefficient [Eqs. (13–15) and Fig. 7]
C_{DWu} = uncorrected drag coefficient for viscous part of model drag (Table 4)
C_{Pc} = corrected pressure coefficient on a model or tunnel surface [Eq. (4)]
C_{Pu} = uncorrected pressure coefficient on a model or tunnel surface [Eq. (4)]
C_S = spacing between solid blockage source and sink
D_{12} = drag of source Q_1 due to velocity U_{12} [Eq. (8)]
D_{21} = drag of source Q_2 due to velocity U_{21} [Eq. (8)]
H = tunnel height
L = length of a side of a flat plate (Fig. 5)
N = shape factor for horizontal buoyancy calculations (Table 1)
Q_A–Q_C = general source or sink strengths (Fig. 1) at arbitrary positions on the tunnel centerline
Q_S, Q_W = source or sink strengths for solid and wake components of theoretical flow model; source $+Q_S$ and sink $-Q_S$ are spaced distance C_S apart with Q_W at center
Q_{WM} = portion of Q_W due to model viscous drag [Eq. (10)]
Q_{WT} = portion of Q_W due to changes in tunnel wall skin friction induced by model [Eq. (10)]
Q_1, Q_2 = source strengths used in deriving cross effects between two sources [Eqs. (7–9) and Fig. 2]
R_{AB}, R_{BC}, R_{AC} = source-to-other-image radii associated with sources A, B, and C; analogous to R_{12} (Table 3)
R_{12} = radius from source 1 to the image of source 2; equals R_{21} [Eqs. (7) and (8) and Fig. 2]
S = model reference area
U_C = corrected velocity at the location of the normal plate (Fig. 5)
U_∞ = tunnel reference velocity
U_{12} = U-component velocity at in-tunnel source Q_1 due to the image of source Q_2 [Eqs. (7) and (8) and Fig. 2]
U_{21} = U-component velocity at in-tunnel source Q_2 due to the image of source Q_1 (Fig. 2)
u = local supervelocity on a model or tunnel surface [Eq. (4)]
X = axial distance from tunnel reference plane
X_A = arbitrary location of solid blockage source Q_S (Table 3)
X_B = arbitrary location of wake source Q_W (Table 3); becomes X_W in later analysis
X_C = arbitrary location of solid blockage sink (Table 3)
X_W = specific location of wake source Q_W obtained from wall pressures (Table 4)
X_1, X_2 = locations of Q_1 and Q_2 on tunnel centerline [Eqs. (7) and (8) and Fig. 2]
ΔC_D = generic increment due to empty tunnel axial gradient [Eq. (5)]
ΔC_{DcM1} = increment using the standard Maskell method [Eq. (14) and Fig. 7]
ΔC_{DcM2} = increment using the two-step Maskell method [Eq. (13) and Fig. 7]
ΔC_{DM} = increment due to presence of model, determined from wall pressures and model viscous drag; includes only interference related to the model wake [Eq. (11) and Table 4]
ΔC_{DMW} = increment due to presence of model, determined only from wall pressures; includes interference related to both model wake and wall boundary-layer effects [Eq. (11a) and Table 4]
$\Delta C_{D\,offset}$ = additive increment associated with the empty tunnel velocity change between the tunnel reference plane and the location of the wake source Q_W [Eq. (1) and Table 4]
ΔC_{DT} = model-induced change in tunnel boundary-layer skin-friction drag, expressed in the same units as model drag coefficient [Eq. (12)]
$\Delta C_{D\,tun1}$ = additive increment due to empty tunnel axial gradient, calculated as model volume times tunnel gradient times shape factor [Eq. (3) and Table 4]
$\Delta C_{D\,tun2}$ = additive increment due to empty tunnel axial gradient, calculated using solid body source and sink, and their separation C_S [Eq. (2) and Table 4]

Presented as Paper 96-0562 at the AIAA 34th Aerospace Sciences Meeting, Reno, NV, Jan. 9–12, 1996; received Feb. 9, 1996; revision received July 10, 1996; accepted for publication July 22, 1996; also published in *AIAA Journal on Disc*, Volume 2, Number 1.

*Staff Specialist, Low Speed Wind Tunnel, 1055 Richardson Road, Smyrna, GA 30080. Associate Fellow AIAA.

ΔD_{offset} = drag correction arising from the offset between the tunnel velocity reference point and the location of the wake source [used in deriving Eq. (1)]

ΔU_{offset} = change in velocity between the tunnel velocity reference point and the location of the wake source [used in deriving Eq. (1)]

ϵ = Maskell's blockage constant [Eqs. (13–15)]

I. Introduction

THE principal tunnel boundary constraint corrections applied to wind-tunnel data concern angle of attack and forward speed. Incremental drag corrections, which are applied prior to these, fall into neither category and have received little attention in the literature. Two unrelated incremental drag corrections will be discussed in this paper, both of which imply induced pressures on the model that are absent in free air. The first increment, found in most wind-tunnel testing texts,[1,2] compensates for axial pressure gradients due to excessive tunnel-empty boundary-layer growth or incorrect test section taper. Because its form is similar to that for hydrostatic lift, it is usually termed horizontal buoyancy. The second increment, designated the wake-induced drag increment, is a function of the viscous drag of the test model and is the main subject of the present paper. Unlike the gradient correction, there is no direct connection to model volume. This concept runs counter to traditional thinking, and alternative derivations have been performed to confirm the result.[3,4]

The recent emphasis on error documentation by AGARD,[5] the International Standards Organization,[6] AIAA,[7] and other organizations has renewed the interest in the present topic. Establishing and documenting the accuracy of tunnel constraint estimates for angle of attack and tunnel speed is a formidable undertaking; the task for gradient effects is even more challenging. Though the other corrections are usually much larger, percentage accuracies may be compromised if the incremental corrections are not handled properly.

In response to this renewed interest, a report was re-released recently that consolidates the results on the topic.[3] Reference 4 employs momentum considerations to derive the wake-induced drag increment directly, rather than the kinematic approach used here and in Ref. 3. A treatment that links the two approaches is presented in Ref. 8.

The derivation of various incremental drag equations will be described in Sec. II of this paper. This will be followed, in Sec. III, by examples of their application. An extension of Maskell's separated flow correction procedure[9] will be described briefly and compared with the present treatment. The principal results will be summarized in Sec. IV.

II. Theoretical Development

A. Introduction

A test object in a wind tunnel may be modeled by singularity methods employing, for example, a system of source and doublet panels distributed over the surface of the body and its wake. The source panels can be used to represent boundary-layer and/or wake displacement surfaces, and the doublet panels represent thickness effects and lift. The thickness model includes closed separation bubbles when these are present. Since tunnel effects require only a far-field representation, the model may be considered as a superposition of simplified closed and open bodies representing solid-body and wake effects, respectively. The wake body is created using a single source, and a source–sink pair creates a long ovoid. In some cases the source–sink pair can be compressed to a doublet. A combined body using the source–source–sink representation is plotted in Fig. 1. The additional sink, located at infinity downstream, is used to return the approach flow to its datum condition.

A number of approaches can be considered for sizing the singularities of Fig. 1. The model's wake source strength Q_W is related to the total viscous drag of the model and can be derived from $C_{D\,\text{vis}}$. The sources $+Q_S$ and $-Q_S$ can be sized and placed appropriately if the model location, effective volume, and fineness are known. There are obvious difficulties in finding the purely viscous drag and in finding the size of the separation bubble(s). The use of wall pressures, suitably interpreted, is one way of avoiding these difficulties.[10–12] This procedure also picks up changes in the model source strength caused by the presence of the tunnel and the effects of changes in the wall boundary layers caused by the presence of the model. Because of the latter, it is still necessary to estimate a model's viscous drag.

The incremental drag caused by the wind tunnel may be determined by considering the velocity field that acts upon the sources of Fig. 1. There are two major contributors. The first velocity field concerns the static gradients that are present with the tunnel empty. These may be caused by test section taper or wall boundary-layer growth, which are usually balanced against one another to some approximation. The residual gradient is part of the tunnel calibration and remains constant throughout a test. The second velocity field is caused by the constraining effects of the tunnel walls upon the flow-field generated by the installed model. This varies with model conditions and may be determined using imaging methods, for example.

Table 1 summarizes the interactions between the imposed flows and the sources and includes results that will be derived later in this section. The first entry in the main table concerns the effect of the static tunnel gradient on a solid body. The multiplier N is the shape factor that depends on the slenderness of the body involved. Setting N to unity implies that pressures may be superposed, which is correct only for small perturbations. For example, the correct analysis for a sphere, using velocity superposition, gives $N = 1.5$ (see Sec. II.B).

The second line of column 1 arises because the location of the wake source, Q_W, is not usually coincident with the tunnel reference point for velocity, being separated by an offset X_B. (Note that this becomes X_W later in the analysis.) The corresponding drag

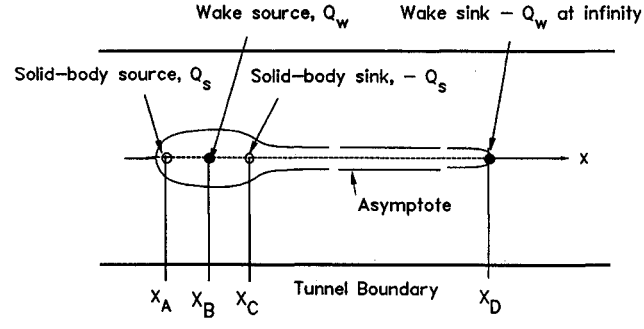

Fig. 1 Model representation in the wind tunnel.

Table 1 Summary of additive gradient-induced drag effects

Gradient induced by ⇒ External effects (e.g., wall taper or empty-tunnel boundary layer) (Sec. II.B)	Model and wake images (Sec. II.C)	
Gradient acts upon ⇓	Solid body plus any separation bubble	Wake displacement body
Solid body plus any separation bubble	$-\frac{N \times \text{volume}}{S}\frac{\partial C_P}{\partial X}$ [see Eq. (6)]	Effects cancel (see Fig. 2)	Equal and opposite to solid images on wake body (see Table 3)
Wake displacement body	$-\frac{Q_W}{U_\infty C}\frac{C}{S}\frac{X_W}{B}\frac{\partial C_P}{\partial (X/B)}$ [see Eq. (1)]	Equal and opposite to wake images on solid body (see Table 3)	$-\frac{1}{2}\frac{Q_W}{U_\infty C}C_{DM\,\text{vis}}$ Wake-induced ΔC_D [see Eq. (11)]

correction will be derived in Sec. II.B. The remaining four entries in Table 1 relate to image effects, which are dealt with in Sec. II.C. The source-image-induced velocities, acting on $\pm Q_S$, produce zero resultant drag for reasons of symmetry. It is also found that the effects of the solid-body images, acting on the wake body, are exactly offset by the effects of the wake images acting on the solid body. The final image term, at the bottom right of Table 1, is the wake-induced drag increment, which is solely wake related. This increment reflects changes in boundary-layer and separation bubble displacement surfaces caused by the wake image system.

B. Estimation of Drag Increment for Externally Generated Pressures

Effect on Wake Source, Q_W

As already indicated, a bookkeeping correction to drag is required to allow for the fact that the calibration point for tunnel velocity and the wake source location are separated by a distance X_B. The velocity change over this distance is X_B times the externally imposed tunnel velocity gradient. Writing

$$\Delta D_{\text{offset}} = \rho \Delta U_{\text{offset}} Q_W$$

and recognizing that

$$\Delta U_{\text{offset}} = \frac{\partial U}{\partial X} X_B \qquad \text{and} \qquad \rho \frac{\partial U}{\partial X} = -\frac{1}{U_\infty} \frac{\partial p}{\partial X}$$

(X derivative of Bernoulli's equation) gives

$$\Delta D_{\text{offset}} = -\frac{1}{U_\infty} X_B Q_W \frac{\partial p}{\partial X}$$

On normalizing and rearranging, this becomes

$$\Delta C_{D\,\text{offset}} = -\frac{Q_W}{U_\infty C} \frac{C}{S} \frac{X_B}{B} \frac{\partial C_P}{\partial (X/B)} \tag{1}$$

and X_B, retained here for generality, becomes X_W in the following wall pressure signature analysis.

Effect on Solid-Body Source and Sink Using the $\rho U Q$ Approach

The effect of tunnel static gradient on the solid body source and sink, $\pm Q_S$, given by a very similar analysis, is

$$\Delta C_{D\,\text{tun2}} = -\frac{Q_S}{U_\infty C} \frac{C}{S} \frac{C_S}{B} \frac{\partial C_P}{\partial (X/B)} \tag{2}$$

Effect on Solid Body Source and Sink Using the Gradient-Times-Volume Approach

The literal interpretation of the horizontal buoyancy drag increment is obtained by integrating imposed pressure with respect to model cross-sectional area, giving

$$\Delta C_{D\,\text{tun1}} = -\frac{\text{model volume}}{S} \frac{\partial C_P}{\partial X} \tag{3}$$

However, a factor that depends on model shape[1,2] should be applied for cases in which the pressure gradient is caused by flow. The proper value for this factor is not always obvious, and it is sometimes omitted. This difficulty may be avoided if velocity superposition is employed.

Rather than superposing pressures, the preferred approach is to use a local mainstream approach that scales model surface velocites in proportion to the corrected mainstream velocity at a specific X station.[11] This leads to Eq. (6.4) of Ref. 11, namely,

$$C_{Pc}(X) = \frac{C_{Pu}(X) - 1}{[1 + u(X)/U_\infty]^2} + 1 \tag{4}$$

where $u(X)$ is the imposed velocity at location X and the various C_P values are measured at the model surface. The corresponding drag increment is found by integrating pressures over the model surface.

It is usually impractical to employ Eq. (4) because pressures are not available or because there are too few for accurate drag integration. One alternative, which also avoids the pressure superposition problem, is to consider the sources, sinks, or doublets that represent the model volume. Considering first a single doublet—representing a sphere of radius R in uniform flow—it is shown in Ref. 3 that

$$\Delta C_D = \frac{2\mu}{\pi R^3 U_\infty} \frac{\partial [U(x)/U_\infty]}{\partial (X/R)} \tag{5}$$

where doublet strength $\mu = 2\pi U_\infty R^3 = 1.5 U_\infty$ times sphere volume. Thus, for a sphere, Eq. (5) becomes

$$\Delta C_D = -1.5 \frac{\text{model volume}}{S} \frac{\partial C_P}{\partial X} \tag{6}$$

The factor of 1.5, relative to Eq. (3), arises because superposition of velocities, rather than pressures, has been employed. The added 0.5 represents the standard result for the virtual mass of an accelerating sphere. The added mass for a sphere is given in Refs. 1 and 2 and for other ovoids is given in Ref. 13. Reference 14 shows that the added mass ratio for a normal circular disk is $(\pi + 2)/\pi$ times that of the enclosing sphere.

The results of applying the preceding equations were compared in Ref. 11 for a 15-in. sphere, placed in a 30 × 43 in. wind tunnel. As a test of the various methods, measured tunnel surface pressures were used when calculating the imposed gradients. The corresponding normal velocities, calculated at the sphere surface using the pressure signature method, were used as boundary conditions in a 648 panel Douglas Neuman solution. This provided a standard for comparison in which the boundary conditions were properly fulfilled.

Table 2 compares the results obtained using the various methods described earlier. Three of these results agree quite well. The exception is the pressure gradient times volume method. The ratio of 1.5 between results using Eqs. (3) and (5) represents the anticipated shape factor.

C. Net Interference Drag Due to Image Effects

A wind-tunnel model may be represented, for blockage interference estimation purposes, by an array of three-dimensional sources arranged along the tunnel axis. The effect of the tunnel walls is represented by a doubly infinite array of images. Figure 2 shows two sources on the axis of the wind tunnel and an image set reflected in the tunnel floor. The images in the tunnel floor are typical of any of the images in the complete set, and so the results obtained later will apply to the entire image array. We are interested in the incremental forces on the two in-tunnel sources, due to velocities induced by both of the images.

The axial velocity at the in-tunnel source Q_1 due to the image of Q_2 is given by

$$U_{12} = \frac{Q_2(X_1 - X_2)}{4\pi[(X_1 - X_2)^2 + H^2]^{1.5}} = \frac{Q_2(X_1 - X_2)}{4\pi R_{12}^3} \tag{7}$$

Table 2 Examples of gradient-induced drag calculations

Method[11]	Eq.	ΔC_D
Paneled sphere	——	0.0216
Volume × press. gradient	(3)	0.0140
Superposed velocities	(4)	0.0202[a]
Doublet str. × vel. grad.	(5)	0.0210

[a]Calculated on a plane 45 deg from the vertical.

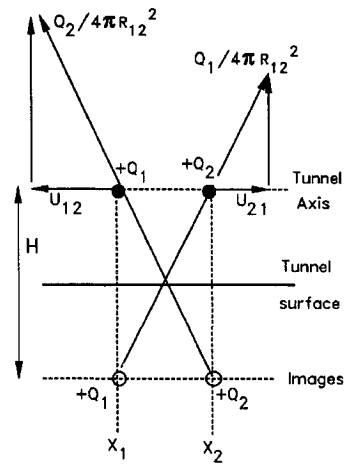

Fig. 2 Effects of source images.

Similarly, the velocity at Q_2 due to the image of Q_1 is

$$U_{21} = \frac{Q_1(X_2 - X_1)}{4\pi\left[(X_2 - X_1)^2 + H^2\right]^{1.5}} = \frac{Q_1(X_2 - X_1)}{4\pi R_{12}^3}$$

By inspection,

$$U_{11} = U_{22} = 0 \tag{7a}$$

Using the fact that the axial force experienced by a source in a stream is $\rho U Q$ (e.g., Ref. 15), we obtain the drag on Q_1 and Q_2 as

$$D_{12} = \rho U_{12} Q_1 = \rho Q_1 Q_2 \frac{(X_1 - X_2)}{4\pi R_{12}^3}$$

$$D_{21} = \rho U_{21} Q_2 = \rho Q_2 Q_1 \frac{(X_2 - X_1)}{4\pi R_{12}^3} = -D_{12} \tag{8}$$

Hence

$$D_{12} + D_{21} = 0 \tag{9}$$

That is, the net force on Q_1 and Q_2, due to the velocities induced by their images, is zero. This is hardly unexpected if $Q_1 = Q_2$ since we are dealing with a closed body and its image in potential flow. Though both sources were on the tunnel axis in the case considered here, it is readily shown that the result is true for any source pair within the tunnel. The net drag increment on the complete set of sources in the test section, due to wall image effects, is therefore zero.

Net Source Strength

If the model in the test section is represented by sources and sinks, their net far-field effect may be obtained by considering a single source whose strength is the sum of all of the individual sources in the test section, including sources that represent model-induced changes in the growth of the tunnel wall boundary layer.

The wake source strength could be obtained, with some difficulty, by estimating all of the individual boundary-layer and wake displacement areas concerned. However, it is more practical to use a direct method to determine the strength, such as the wall pressure signature approach.[10–12] It is important to distinguish displacement effects due to a model's viscous wake from those associated with net changes in the tunnel boundary layer, the combined effects of which are sensed by tunnel wall pressures. Therefore, we write

$$Q_W = Q_{WM} + Q_{WT} \tag{10}$$

for the model and tunnel viscous effects, respectively.

Effect of the Downstream Sink on Drag Increment

In a wind tunnel of cross-sectional area C, the presence of the source Q_W in the test section gives rise to an asymptotic upstream-directed velocity $-\frac{1}{2}(Q_W/C)$ at far upstream locations and a corresponding downstream-directed velocity $+\frac{1}{2}(Q_W/C)$ at far downstream locations. Since, by definition, the upstream reference conditions are not affected by the presence of the model, a sink of strength Q_W is added to the theoretical interference model far downstream. This returns the upstream velocity to its datum value of U_∞. A source body is created in the test section that becomes parallel sided and closes behind the downstream sink at infinity. The flow accelerates from a velocity of U_∞, upstream, to $U_\infty + \frac{1}{2}Q_W/C$ at the location of Q_W and then to an asymptotic value of $U_\infty + Q_W/C$ where the body becomes parallel sided. Corresponding decreases in static pressure are seen.

Knowing that the $\frac{1}{2}(Q_W/C)$ velocity increment at the model acts on $Q_{WM} + Q_{WT}$, we may evaluate the corresponding interference drag increments, again using the $\rho U Q$ result. The incremental drag on the model becomes

$$\Delta D_M = \tfrac{1}{2}\rho(Q_W/C)Q_{WM}$$

which leads to

$$\Delta C_{DM} = \tfrac{1}{2}(Q_W/U_\infty C)C_{DM\,\mathrm{vis}} \tag{11}$$

where $C_{DM\,\mathrm{vis}}$ is estimated from balance measurements by subtracting vortex drag from the total. In the absence of drag measurements, the full Q_W may be used, recognizing that the resulting drag increment will be slightly high because changes in the tunnel boundary layers are included. In this case, Eq. (11) becomes

$$\Delta C_{DMW} = (C/S)[Q_W/U_\infty C]^2 \tag{11a}$$

The increment in tunnel boundary-layer drag

$$\Delta D_T = \tfrac{1}{2}\rho(Q_W/C)Q_{WT}$$

or

$$\Delta C_{DT} = \tfrac{1}{2}(Q_W/U_\infty C)\Delta C_{DT\,\mathrm{vis}} \tag{12}$$

can be evaluated as a difference but is usually of little interest.

Cancellation of Wake-on-Solid by Solid-on-Wake Terms

The generalized drag result of Eq. (8) may be applied to the full source–source–sink set of Fig. 1, giving the nine terms displayed in Table 3. Each row represents a source or a sink situated at X_A, X_B, or X_C on the tunnel axis (Fig. 1). The columns represent the images of this set. The signs of the sources and the sequence of the terms have been left in their original form to show how cancellation occurs. It will be noticed that the leading diagonal of the table contains zeros [see Eq. (7a)].

The most striking feature of Table 3 is that diagonal terms cancel, in accordance with the general result of Eq. (9). This means that the resultant drag of the nine terms shown is zero. In particular, the wake image effects on the solid-body source and sink (middle column) cancel exactly with the solid-body source–sink effects on the wake source (middle row). This confirms the result discussed earlier (Table 1), and leaves the wake terms of Eqs. (9) and (10) as the only contributors to the wake-induced drag increment.

Although the tunnel wall images of model sources, sinks, and solid-body doublets do contribute to tunnel dynamic pressure corrections, the preceding analysis shows that they do not contribute to incremental drag corrections. It follows that body volume related drag increments, found in many text books, are valid only in connection with externally applied, model-independent gradients such as those due to test section taper.

Table 3 Diagonal cancellation of interference terms

Image of ⇒ Acting on ⇓	Q_S (at X_A)	Q_W (at X_B) wake image on solid ⇓ body ⇓	$-Q_S$ (at X_C)
Q_S	0	$\rho Q_S \dfrac{Q_W(X_A - X_B)}{4\pi R_{AB}^3}$	$\rho Q_S \dfrac{(-Q_S)(X_A - X_C)}{4\pi R_{AC}^3}$
Q_W Solid image(s) on wake body ⇒⇒	$\rho Q_W \dfrac{Q_S(X_B - X_A)}{4\pi R_{AB}^3}$	0	$\rho Q_W \dfrac{(-Q_S)(X_B - X_C)}{4\pi R_{BC}^3}$
$-Q_S$	$\rho(-Q_S)\dfrac{Q_S(X_C - X_A)}{4\pi R_{AC}^3}$	$\rho(-Q_S)\dfrac{Q_W(X_C - X_B)}{4\pi R_{BC}^3}$	0

III. Application of Increments

A. Flow Physics

The most important application of the preceding results is to high-drag models, especially if they have significant areas of separated flow. Tunnel-imposed flowfields interact with the separation bubbles and change their shape. Figure 3 illustrates this for a two-dimensional cylinder, with a typical wake, in a tunnel whose height is two cylinder diameters. Instead of bulging upwards, the upper streamline (upper plot) is constrained by the tunnel to remain straight. The lower plot shows the flowfield that is impressed on the free airflow by the tunnel. The X dimension is compressed to emphasize the streamline shapes and the bare cylinder appears as a vertical ellipse. It can be seen from the streamlines (Fig. 3, lower plot) that the imposed flow accelerates to a maximum just downstream of the cylinder's crest and then decelerates. The velocity imposed downstream exceeds the upstream value because of the wake displacement effect. There is also a vertical inflow that reaches a maximum just aft of the cylinder, but this appears to be of less significance.[3] Figure 3 is an extreme case, but it is likely that three-dimensional cases will be qualitatively similar.

Tunnel effects on the separation bubble behind a normal flat plate are sketched in Fig. 4. Reference 3 shows that the most significant feature of the imposed tunnel flow is the increased velocity at the separation point and the corresponding increase in shear layer strength at separation. This can be accommodated by the appropriate dynamic pressure correction. However, there is also a tunnel-induced acceleration in the streamwise velocity, beyond this point, that strengthens the shear layer further (see 1 and 2 in Fig. 4). Being stronger, the vortical sheet closes more rapidly in the tunnel than in free air (see 3 and 4) and the separation bubble is smaller. Consequently, the base pressure is reduced (see 5) and the drag increases.

Figure 5 shows experimental data that demonstrate the aforementioned changes in bubble geometry. A series of square normal plates was tested in the Lockheed 23.25 × 16.25 ft (7.087 × 4.953 m) wind tunnel, ranging in size from 3 ft (0.91 m) to 6 ft (1.83 m) square. The pressure signature method was used to determine the effective wake and solid bodies as a function of model size. The ordinate in Fig. 5 is the effective doublet strength $Q_S C_S$, which, in broad terms, may be

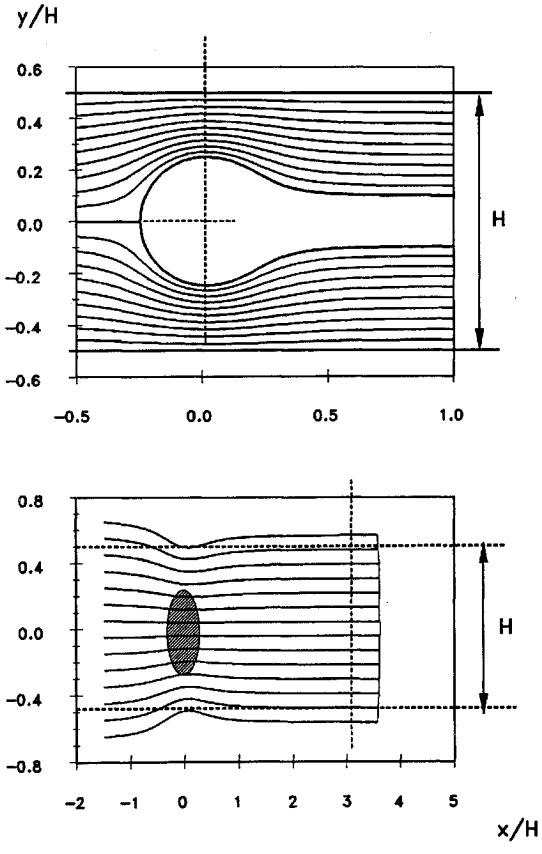

Fig. 3 Tunnel-induced flow on a cylinder and its wake.

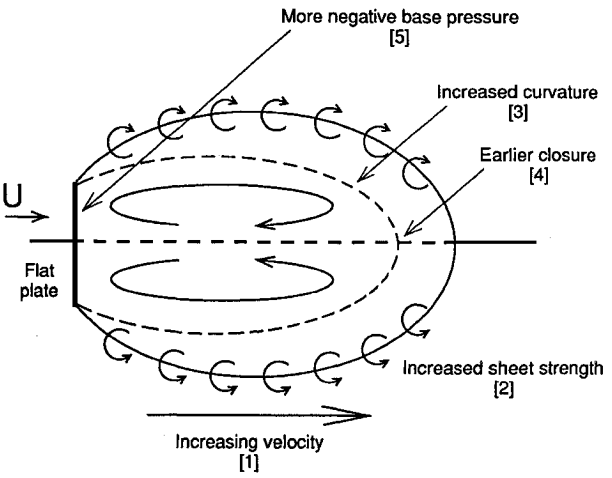

Fig. 4 Deformation of a separation bubble by tunnel-induced flows.

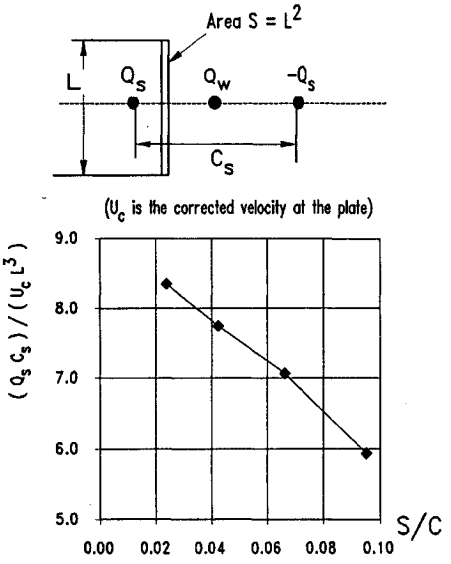

Fig. 5 Experimental demonstration of bubble size reduction by tunnel-induced flows.

thought of as representing an equivalent sphere. After normalization using plate size and corrected velocity at the plate, Fig. 5 shows that this quantity is some 25% smaller for the largest tested plate than for the smallest. This shows that the tunnel-induced changes to the bubble are very significant. Normalization on U_C, the corrected velocity at the plate, is important because it distinguishes the dynamic pressure correction, which sets up the shear layer strength at separation, from the subsequent acceleration and changes in bubble shape.

Because the bubble shape is changed, tunnel correction is more than a matter of correcting for tunnel-induced velocity changes at the separation point. In fact, an obvious question arises as to whether data that involve flow geometry changes can be corrected. It will be demonstrated that the answer to this question is yes, provided that the location of the separation point is unchanged by wind-tunnel constraint. This is clearly not a problem for a normal flat plate.

B. Relationship to Maskell's Method

There is precedent for dealing with changed-shape separation bubbles in the work of Maskell.[9] Using axial momentum considerations, he deduces a result in which the base pressure in a separated region characterizes the correction. He also gives a related, drag-based result. In his development, Maskell clearly acknowledges that wake distortion is involved.

As indicated earlier, the wake-induced drag increment, whether associated with bubble distortion or not, should be applied before the dynamic pressure correction. The fact that Maskell's procedure is a one-step process blurs this distinction. In Ref. 3, Hackett recasts the

Table 4 Additive drag corrections for high-drag test models

Description ⇒ Quantity ⇓	Square flat plate, 5 × 5 ft	Fighter model A, high α	Fighter model B, high α	Sport utility vehicle, full scale	Typical sedan, full scale
Measurements					
Ref. area, ft^2	25.0	24.0	7.0	27.58	23.42
Ref. length B, ft	23.25	23.25	23.25	32.5	32.5
S/C, %	6.62	6.35	1.85	7.30	6.20
C_{DWu}	1.500	1.65	1.57	0.72	0.33
$C_{DWu}S/C$, %	9.93	10.48	2.91	5.26	2.04
Flow model					
$Q_W/U_\infty C$	0.065	0.086	0.025	0.048	0.026
X_W/B	0.076	(0.043)[a]	(0.043)[a]	(0.031)[a]	0.022
$Q_S/U_\infty C$	0.219	N/A	0.044	0.082	0.066
C_S/B	0.503	N/A	0.340	0.360	0.369
Tunnel gradient					
$\partial C_P/\partial(X/B)$	−0.0116	−0.0116	−0.0076	−0.0175	−0.0175
$\Delta C_{D\,\mathrm{tun1}}$	−0.0031[b]	−0.0002	−0.0001	−0.0060	−0.0070
$\Delta C_{D\,\mathrm{tun2}}$	−0.0193	N/A	−0.0062	−0.0070	−0.0070
$\Delta C_{D\,\mathrm{offset}}$	−0.0008	(−0.0006)[a]	(−0.0004)[a]	(−0.0004)[a]	−0.0002
Wake-induced inc.					
ΔC_{DM}	−0.0488	−0.0710	−0.0190	−0.0173	−0.0044
Percentage of C_{DWu}	−3.25	−4.30	−1.31	−2.40	−1.33
ΔC_{DMW}	−0.0638	−0.1164	−0.0338	−0.0316	−0.0109
Percentage of C_{DWu}	−4.25	−7.12	−2.15	−4.39	−3.30

[a] Q_W location unknown. Values for $X_W = 1$ ft are shown. [b] Using equivalent disk/sphere volume result.

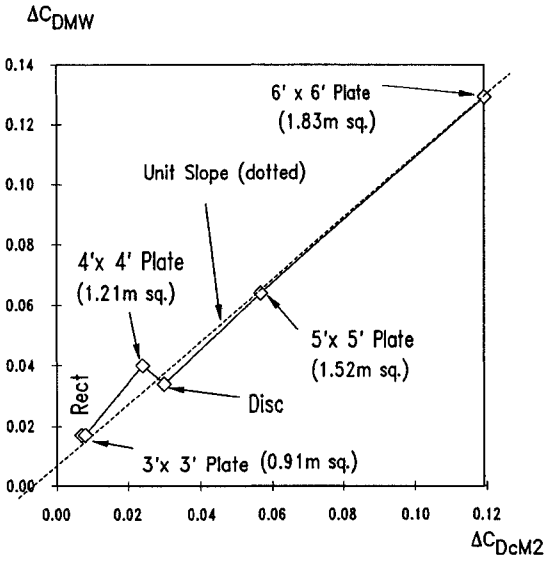

Fig. 6 Drag increments for normal flat plates by Maskell and pressure signature methods.

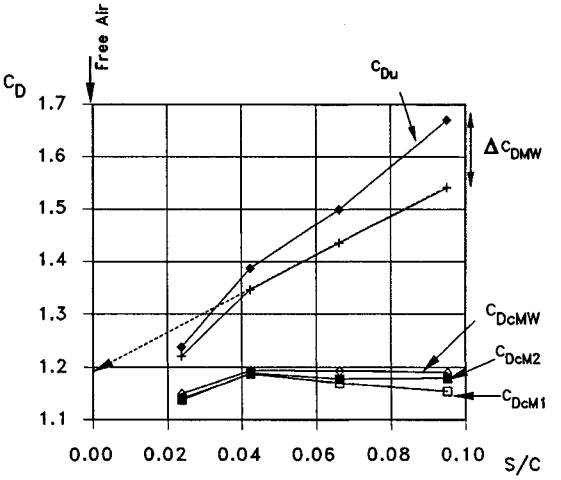

Fig. 7 Blockage corrections for normal flat plates.

Maskell result as a two-step process and shows that overcorrection should be expected when using the original version. This is, in fact, borne out in practice. The corrected drag coefficient, using the two-step Maskell procedure, is defined in Ref. 3 as follows:

$$C_{DcM2} = \frac{C_{Du} + \Delta C_{DM1}}{1 + \epsilon C_{DcM1}(S/C)} \tag{13}$$

where

$$\Delta C_{DM1} = \frac{C_{DcM1} - C_{Du}}{1 + \epsilon C_{DcM1}(S/C)} \tag{14}$$

and

$$C_{DcM1} = \frac{C_{Du}}{1 + \epsilon C_{Du}(S/C)} \tag{15}$$

Equation (15) is the single-step Maskell correction of Ref. 9. The empirical parameter ϵ assumes a value of 2.77 for square normal plates and is a function of bubble aspect ratio.

Figure 6 shows the correlation between the two-step Maskell drag increment of Eq. (14) and the total wake-induced drag increment, $-(C/S)(Q_W/UC)^2$. Being, in effect, the sum of Eqs. (10) and (11), the latter includes both model and tunnel boundary-layer terms. This is appropriate for the present correlation because Maskell's method is unable to distinguish between the two. Except for a slight offset, almost one-to-one agreement is seen in Fig. 6.

C. Application to Normal Plates and Other Models

Figure 7 shows the overall drag correction results for the four normal plates described earlier. The abscissa is plate-to-tunnel area ratio. The uncorrected data, shown by filled diamond symbols, range from 1.238 for the smallest plate to 1.670 for the largest. The lowest point, for the 3-ft (0.91-m) plate, appears to be inaccurate. The + symbols in Fig. 7 show the result after the wake-induced drag increment has been subtracted. If the upper three points of this curve are extrapolated to zero S/C, the free air case, a drag coefficient between 1.19 and 1.20 is obtained (see dotted arrow). (This procedure is preferred because Q_W is found to be proportional to S/C; ΔC_D is proportional to Q_W^2, and so subtracting it from C_{Du} removes a quadratic term.) This should be compared with 1.17 to 1.18, which is usually regarded as the standard range.

With perfect data and perfect correction, the three lower curves in Fig. 7, which show fully corrected data, would be horizontal lines. The original Maskell procedure (open squares) overcorrects slightly, as already mentioned. The curves for both the two-step Maskell procedure (filled squares) and the wake-induced drag increment procedure (open diamonds) are almost horizontal and agree quite well with the projection of partially corrected data. Reference 4 reports similar results for a more varied and more extensive data set.

Table 4 shows examples of drag increment calculations for selected tests in the Lockheed 23.25 × 16.25 ft (7.087 × 4.953 m)

wind tunnel. Errors in the conference version have been corrected. Definitions of the additive drag corrections (i.e., the negative of the increments in the main text) are as follows:

$$\Delta C_{D\,\mathrm{tun1}} = \frac{\text{model volume}}{S}\frac{\partial C_P}{\partial X} \quad \text{[Eq. (3)]}$$

$$\Delta C_{D\,\mathrm{tun2}} = \frac{Q_S}{U_\infty C}\frac{C}{S}\frac{C_S}{B}\frac{\partial C_P}{\partial (X/B)} \quad \text{[Eq. (2)]}$$

$$\Delta C_{D\,\mathrm{offset}} = \frac{Q_W}{U_\infty C}\frac{C}{S}\frac{X_W}{B}\frac{\partial C_P}{\partial (X/B)} \quad \text{[Eq. (1)]}$$

$$\Delta C_{DM} = -\tfrac{1}{2}(Q_W/U_\infty C)C_{DM\,\mathrm{vis}} \quad \text{[Eq. (11)]}$$

$$\Delta C_{DMW} = -(C/S)[Q_W/U_\infty C]^2 \quad \text{[Eq. (11a)]}$$

The two generic fighter models represent larger-model and smaller-model cases, of different design, in tests at high angle of attack (i.e., in excess of 60 deg). The 5 × 5 ft (1.524 × 1.524 m) normal flat plate of the previous section provides a frame of reference. The corrected drag coefficient (not shown) was significantly greater for fighter B than for fighter A. Plan-view reference areas are used for these cases.

The sport utility and sedan represent a high drag and a more typical example of road vehicle testing. As is conventional for car testing, cross-sectional reference areas are used and, being a ground-effect test, the reference tunnel width is twice the actual tunnel height.

Not all of the wake source positions were available for Table 4. However, in most of the cases shown, the horizontal buoyancy drag increment is noticeably smaller than the wake-induced drag increment. Horizontal buoyancy effects would be more noticeable for larger models and in tunnels with greater empty-tunnel gradients.

The tunnel gradient corrections are not part of the pressure signature result because empty-tunnel pressures are taken out of the model-in wall measurements. The different empty-tunnel gradients in Table 4 reflect historical changes to the tunnel breathers or, for the cars, the fact that the models were floor mounted. In all cases, the gradient was negative, giving excessive drag and a negative additive increment. Values of $\Delta C_{D\,\mathrm{tun1}}$ are in most cases smaller than those of $\Delta C_{D\,\mathrm{tun2}}$, which for the fighters, reflects the fact that actual volumes were used for $\Delta C_{D\,\mathrm{tun1}}$, without the separation bubbles. The good agreement between $\Delta C_{D\,\mathrm{tun1}}$ and $\Delta C_{D\,\mathrm{tun2}}$ for cars reflects the use of empirical factors for car volume, which is obtained as cross-sectional area times length times an empirical factor. This factor varies from 0.75 for a sedan to 0.95 for a van.

Two forms of wake-induced drag increments are shown. The first, ΔC_{DW}, is the correct value that employs wake-image-induced velocity and model-only wake drag. The second, ΔC_{DMW}, is the drag increment that includes effects at the tunnel walls as well as at the model. The difference between ΔC_{DM} and ΔC_{DMW}, which represents effects on the tunnel boundary layer, can equal several percent of the uncorrected drag coefficient. This demonstrates the importance of using the viscous drag coefficient and Eq. (10) rather than the simpler result of Eq. (11a). Note that the percentages given in Table 4 are based on uncorrected drag, which, in some cases, can be as much as 50% more than the corrected drag. Expressed in terms of corrected viscous drag coefficient, the values shown would be correspondingly larger.

IV. Conclusions

Incremental drag corrections, applied to wind-tunnel data prior to other corrections, fall into two distinct categories: horizontal buoyancy and wake-induced drag increment. These are discussed, and important distinctions are drawn between them. Examples of applications to normal flat plates and other high-drag test models are given. The work leads to the following conclusions.

1) The gradient-times-volume form of the horizontal buoyancy correction is valid only in connection with externally applied, model-independent streamwise gradients such as those associated with test section taper.

2) The preceding form for horizontal buoyancy, derived using pressure superposition, underestimates the correction if no shape factor is applied. Use of velocity superposition for a sphere, for example, gives a result 1.5 times higher.

3) Wake-image effects on the theoretical solid body model cancel exactly with the effects of solid body images on the wake body. It follows that, contrary to traditional thinking, model-image-induced gradients should not be applied in the gradient-times-volume form.

4) The wake-induced drag increment is a residual wake-on-wake term whose magnitude can be several percent of a model's viscous drag. When derived solely from wall pressures, it includes the effects of changes in tunnel wall skin friction caused by the presence of the model. The increment acting on the model can be extracted by using its viscous drag coefficient.

5) There is a one-to-one correlation between the wake-induced drag increment and a corresponding increment derived from Maskell's method. Both correct for the effects of tunnel induced changes in separation bubble size.

6) The present result for the drag increment due to wake-induced gradient differs from earlier results in that tunnel-induced changes in wake source strength are included in the new analysis.

7) A reduction in relative bubble size of approximately 25% was found on increasing the size of a normal plate from 2.4 to 9.5% of tunnel area.

Acknowledgment

The author is deeply indebted to Derek Wilsden, of Lockheed Martin, for his help in critiquing the present paper and at numerous other times over the past 25 years. We wish him all the very best for a long, healthy, and happy retirement.

References

[1]Rae, W. H., Jr., and Pope, A., *Low Speed Wind Tunnel Testing*, Wiley, New York, 1984, p. 362.

[2]Pankhurst, R. C., and Holder, D. W., *Wind Tunnel Technique*, Pitman, London, 1965, p. 378.

[3]Hackett, J. E., "Tunnel-Induced Gradients and Their Effect on Drag," Lockheed Georgia Co., Lockheed Engineering Rept. LG83ER0108, Marietta, GA, June 1983 (revision of Sept. 1994 available from the author).

[4]Anon., "Wind Tunnel Wall Corrections," AGARDograph 336 (in preparation).

[5]Anon., "Quality Assessment for Wind Tunnel Testing," AGARD Advisory Rept. 304, July 1994.

[6]Anon., "The International Standard, ISO 9001 1994. Quality Systems—Model for Quality Assurance in Design, Development, Production, Installation and Servicing," International Standards Organization, Geneva, Switzerland, 1994.

[7]Anon., "Assessment of Wind Tunnel Data Uncertainty," AIAA Standard, AIAA S-071-95, AIAA, Washington, DC, June 1995.

[8]Cooper, K. R., et al., "Closed Test Section Wind Tunnel Blockage Corrections for Road Vehicles," Society of Automative Engineers, SAE SP 1176, Warrendale, PA, May 1995, p. 78.

[9]Maskell, E. C., "A Theory of Blockage Effects on Bluff Bodies and Stalled Wings in a Closed Wind Tunnel," Aeronautical Research Council, ARC R&M 3400, London, Nov. 1963.

[10]Hackett, J. E., and Wilsden, D. J., "Estimation of Wind Tunnel Blockage from Wall Pressure Signatures: A Review of Recent Work at Lockheed-Georgia," AIAA Paper 78-828, April 1978.

[11]Hackett, J. E., Wilsden, D. J., and Lilley, D. E., "Estimation of Tunnel Blockage from Wall Pressure Signatures: A Review and Data Correlation," NASA CR-152,241, March 1979.

[12]Hackett, J. E., Wilsden, D. J., and Stevens, W. A., "A Review of the 'Wall Pressure Signature' and Other Constraint Correction Methods for High Angle-of-Attack Tests," AGARD Rept. 692, May 1980.

[13]Thwaites, B., *Incompressible Aerodynamics*, Oxford Univ. Press, Oxford, England, UK, 1960, p. 401.

[14]Lamb, H., *Hydrodynamics*, 6th ed., Dover, New York, 1945, pp. 124, 139, and 155.

[15]Prandtl, L., and Tietjens, O. G., "Applied Hydro- and Aeromechanics," Article 79, Dover, New York, 1957, p. 121.